Exploring Sources of Contamination in *Kepler* Surveys for Stellar Rotation

Undergraduate Honors Research Thesis

Presented in Partial Fulfillment of the Requirements for Graduation *with Honors Research Distinction* in Astronomy and Astrophysics in the Undergraduate Colleges of The Ohio State University

By

Rachel Arielle Cannata

The Ohio State University

April 2017

Project Advisor: Dr. Donald M. Terndrup, Department of Astronomy

Table of Contents

Abstract

Large scale surveys, such as *Kepler*, have measured thousands of rotation periods for stars in various evolutionary states, providing plenty of data for studies on rotational spin-down. Current models of rotational evolution due to magnetic braking model all stars as single. However, these models may not be accurate in the rapidly rotating regime because they fail to consider the different evolution of stars in close or tidally synchronized binaries. Additionally, *Kepler*'s broad pixels introduce possible sources of contamination (period misattribution) from fainter stars near or collinear with the target, which could be contributing a fraction of the light but all of the variability. I present an ongoing pilot study on the extent of contamination and binarity among the rapidly rotating (P < 10 days) portion of the García et al. (2014) sample of subgiants, as determined by spectral energy distribution excesses and a radial velocity survey. We find that 4% of subgiants have W4 excess, but none show W2 or W3 excess indicative of secondary stars. To a precision of 40 km/s we find no binaries, but as we work on a complex wavelength calibration we hope to increase precision to 10 km/s and reexamine the data.

1. Introduction

It has long been known that stars lose angular momentum as they age (Skumanich 1972). When they are born, stars have rotation periods on the order of hours, yet slow to periods on the upwards of hundreds of days by the end of their main sequence life time (Epstein and Pinsonneault 2014, Barnes et al. 2016). In part, this slowing is due to the interaction of stellar winds and the star's magnetic field, a process that is not yet fully understood (Matt, MacGregor, Pinsonneault, and Greene 2012). Assuming rotational spin-down follows a Skumanich-like power law (1972), where period is proportional to age $^{-0.5}$, consistently over the main sequence lifetime of the star, a star's age could be inferred from its rotation period, a method which Barnes coined "Gyrochronology" (Barnes 2013, Epstein and Pinsonneault 2014). However, it has become increasingly clearer that Gyrochronolgy produces very approximate ages and that spin-down is not as simple as previously thought (van Saders and Pinsonneault 2013, van Saders, Pinsonneault, García, and Ceillier 2015). A star's effective temperature, for example, can drastically affect its magnetic field (stars with $T_{eff} > 6250$ K do not have a large enough convective envelope for magnetic braking), minimizing the drag which causes the star to slow (van Saders, Pinsonneault, García, and Ceillier 2015).

Though gyrochronological endeavors have not proved as accurate as hoped, there is still a lot to be learned about the mechanics of rotational spin-down. In order to carefully study these dynamics, accurate rotation periods and ages of stars both in clusters and the field are absolutely essential. Cluster surveys produced a plethora of ages and rotation periods for young stars, but older field stars were overlooked.

However, *Kepler* monitored more than 150,000 stars, many of which are subgiants, for six years producing light curves useful for calculating rotation periods from modulation caused by star spots. When combined with age estimates from asteroseismology there is enough rotation-age data for a robust study on angular momentum transport and rotational spin-down in stars.

In addition to the prospect of large-scale angular momentum studies, the other motivating factor for this work is the curious presence of rapid rotators (P < 10 days) among the subgiant population of the García et al. (2014) sample of 540 *Kepler* targets. Despite being old (age > 2 Gyr), evolved stars, approximately 13% of the subgiant population have rapid rotation periods. One way to stay spinning faster longer is to be in a tidally synchronized binary because orbital and spin angular momenta are coupled.

Consider a tidally synchronized binary system consisting of two solar mass stars on a 7-day orbit. Assuming the star spins as a solid body with evenly distributed mass, we know $L = I\omega$. For a uniform density solid sphere $I = 0.4\ MR^2$, $\omega = \frac{v}{R} = \frac{2\pi}{P}$. Since stars are much more centrally concentrated the constant term in the moment of inertia is much smaller, but we will use it as a scaling factor. Putting this all together we get $L = \frac{4\pi M}{5P} R^2$. Scaled to solar mass and radius,

$$L_{rot} = 1.59\text{x}10^{43}\ \text{kg m}^2\ \text{s}^{-1} \left(\frac{c}{0.4}\right) \left(\frac{M}{Msun}\right) \left(\frac{R}{Rsun}\right)^2 \left(\frac{P}{7\ d}\right)^{-1} \quad (1)$$

For a circular orbit, $v = \frac{2\pi a}{P}$ and $L = M_p V R = M_p R \frac{2\pi (G (Mp+Ms))^{1/3}}{(P\ 4\pi^2)^{1/3}}$, where M_p is the mass of the primary star and M_s is the mass of the secondary.

$$L_{orb} = 3.45 \times 10^{44}\ \text{kg m}^2\ \text{s}^{-1} \left(\frac{M}{Msun}\right)\left(\frac{R}{Rsun}\right)\left(\frac{P}{7\ d}\right)^{-1/3}\left(\frac{Mp+Ms}{2\ Msun}\right)^{1/3} \quad (2)$$

Taking the ratio of these two we find

$$\frac{L_{orb}}{L_{rot}} = 21.7\ \left(\frac{c}{0.4}\right)^{-1}\ \left(\frac{R}{Rsun}\right)^{-1}\left(\frac{P}{7d}\right)^{\frac{2}{3}}\ \left(\frac{Mp+Ms}{2\ Msun}\right)^{\frac{1}{3}} \quad (3)$$

In reality, stars are a lot more centrally concentrated than what can be approximated by a uniform density sphere. As such, c, the constant in the moment of inertia, is about 6 times smaller than 0.4. Equation 3 is a lower limit on the amount of angular momentum tied up in the orbit versus rotation. Most of the angular momentum in this system is contained in the orbit, meaning that conventional ways of losing angular in single stars must now also carry away angular momentum from the orbit, keeping the system spinning fast for longer periods of time. Tidally synchronized binaries could mask themselves as single star rotation due to the nonuniform surface temperature gradient caused by tidal distortions. As the system rotates, the brighter and fainter portions of the star produce periodic modulations, which then get picked up by *Kepler*. Alternatively, the companion could be the spotty star whose modulation is detected and attributed to the target.

Binaries are one such possible contaminant in the García sample but contamination can take other forms. *Kepler*'s defocused cameras captured images with 4" per pixel resolution, drastically increasing the target PSF and masking any faint stars near it. These stars, in either a chance superposition or within 4" of the target, could be contributing most or all of the variability *Kepler* detected despite contributing only part

of the light. Studies on contamination and false positive rates in *Kepler* data have been done before, but in the context of finding exoplanets (Atkinson et al 2017**,** Dalba, Muirhead, Croll, Kempton 2017) These studies report crowding rates of about 14.5 % within 4" of the target which support the plausibility of getting chance superpositions of stars. Studies on rotation contamination, however, remain scarce. Since accurate rotation periods are critical for understanding wind driven spin-down, it is imperative to ensure that the stars we study are indeed what we think they are, namely, singular subgiants. Current models of stellar rotational evolution treat all stars as single. Knowing the binary fraction of the rapidly rotating subgiant population is crucial because allows us to see if there is a large enough population to study spin-down and potentially affect rotational evolution models.

In order to fill the gap of contamination studies in the *Kepler* rotation data, to ensure accurate rotation periods for studies of angular momentum loss, and understand why 13% of our subgiant population are rapidly rotating, this work explores the possibility of misattribution of rotation period from a variety of sources. This is also a pilot study for PhD candidate Gregory Simonian, whose dissertation will focus on binary contamination for a much larger sample of stars. For the success of his project we need to know whether OSMOS is capable of capturing high-resolution spectra. Section 2 of this thesis covers our sample selection and methodology. Section 3 covers our photometric and spectroscopic analysis. Section 4 discusses our conclusions and section 5 covers future work. For reference, all figures and tables can be found at the end of the paper.

2. Methodology

We focused on a sample of 25 rapidly rotating subgiants selected from the García et al. (2014) sample of 540 *Kepler* stars. Table 1 shows the complete list of targets, their rotation periods as calculated by García et al., and the type of data (photometric or spectroscopic) we have for that star. Figure 1 shows our sample's characteristics, T_{eff} and Log g, compared to the entire García et al. subgiant population.

2.1 Detection of modulating companions through photometry

From UT 26 05 2015 through UT 17 06 2015 I took nearly 35,000 BVRI images of 25 *Kepler* targets using Andor, a frame transfer CCD with 0.27" per pixel resolution attached to the 1.3 meter McGraw-Hill Telescope at the MDM Observatory on Kitt Peak. The primary goals of this run were twofold: to identify and do photometry on the target and stars within 5" from the target and to accurately get the position of the target to test how well Andor and the 1.3m telescope could collect images for centroid analyses. Should another star's light be blended into the target, we would expect the centroid of the target to shift as that secondary star was varying. For each star, depending on its brightness, we took 1 - 5 second exposures in rapid succession for about 120 seconds. For each stack of images we can calculate the shift in centroid from one set of exposures to another looking for periodic movement, but in order to do so we must have a firm grasp on how the star shifts from single exposure to exposure due to atmospheric effects. Figure 2 shows the average shift in position from image to image and the worst shift in position, both in arcseconds. For the entire observing run seeing varied between 1.1 and 2.1 arcseconds.

We calibrated our instrument with a series of Landolt standard stars (Table 2) to produce a photometric solution for each filter since the way Andor detects light varies from filter to filter (Landolt 2007). During our two photometric nights (out of 20 clear nights), we took BVRI images of each of standard to see how well we reproduced their magnitudes after image processing. Table 3 has our calculated colors from UT 06 14 2015. Figure 3 shows our instrumental b-v against catalog B-V values. Instrumental magnitudes were calculated by

$$-2.5 * \log(\text{counts/s}) + \text{constant}$$

Though fairly linear, we still needed the following corrections (here lowercase letters represent instrumental magnitudes, uppercase are catalog values and X is airmass):

$$V = v + 0.025\,(b - v) - 0.165\,X + \text{const.}$$

$$B - V = 1.176 * (b - v) - 0.086\,X + \text{const.}$$

$$V - R = 1.125 * (v - r) - 0.044\,X + \text{const.}$$

$$V - I = 0.967 * (v - i) - 0.076\,X + \text{const.}$$

This calibration was essential for two reasons. First, we combined our BVRI photometry with JHK and W1-4 photometry from 2MASS and WISE[1] to form composite spectral energy distributions (SEDs) for all 25 stars. Any excess flux indicates the presence of some cool object contributing light near or in the same line of sight as the target. Second, we are in the process of doing photometry for the target and any stars within 5" of the target, to account for *Kepler's* broad pixels, to see which of the stars is actually doing the varying attributed to the target. I processed all of the images in 2015 and we are currently working on a script to rapidly do the photometry. Analysis is set for

[1] Data retrieved from http://irsa.ipac.caltech.edu/applications/Gator/

2017. For any stars in a chance superposition with the target we can also analyze centroid movement to see if that hidden, collinear star is actually doing the varying. We would expect to see the center of the target's PSF to shift if the other star was getting brighter and fainter as it rotated.

2.2 Finding binaries through spectral Doppler shifts

Should our target actually be in a binary system, we would expect to see periodic Doppler shifts in each star's spectra. From UT 05 18 2016 through 06 03 2016 we took multi-epoch spectra of a 21-star sample, for which we already had photometry, of the García et al rapid rotators using the Ohio State Multi-Object Spectrograph (OSMOS) on the 2.4 meter Hiltner telescope at the MDM Observatory on Kitt Peak. Each exposure lasted 240 - 300 seconds depending on the target's magnitude. OSMOS is highly sensitive to camera focus, flexure, and temperature resulting in varied curvature of spectral lines as a function of focus. This curvature also varies as a function of y position on the spectrograph, with lines spreading out the further they are from the middle of the detector (Schulze 2017). To map out these dependences we took Hg-Ne arc spectra at various positions on the sky and at different camera foci to account for flexure and line spreading due to changing focus. The top panel of figure 4 shows pixel shifts of both the Telluric line and Hg-Ne emission lines over changing hour angle during one night of data collection (UT 20 05 2016). Residuals from the linear fit are about 0.09 pixels. The bottom panel shows the same shifts but instead plotted as radial velocity (RV) shifts versus degrees.

Correcting for just flexure is not enough, though. If all wavelengths were shifted in the same way due to flexure then we would be able to measure the shift of a stationary

line, like the Telluric line, and then correct for it over all wavelengths. However, after this shift is accounted for, there are still wavelength-dependent effects. Figure 5 shows the radial velocities of stationary lines from an Hg-Ne arc spectrum. Each of the five major emission features is plotted against the radial velocity measured for that line, but there are two main things to note: arc lamp emission lines should not have radial velocities, and they do not all have the same velocity, implying there is some sort of secondary effect that is wavelength-dependent. As mentioned earlier in this paper, the other effects are spectrograph temperature and camera focus, with focus increasing as temperature decreases. This is clearly visible when we look at the dispersion, which is a measure of Angstroms per pixel and is critical for mapping spectra from pixel to wavelength space. OSMOS' dispersion is about 0.723 Å/pixel, but it changes linearly with changing focus and temperature. Figure 6 shows the changing dispersion over the course of the observing run. The top panel shows dispersion in Angstroms per pixel as function of temperature from one night and the bottom panel shows dispersion as a function of focus over multiple nights. The lower the dispersion, the better the resolution and understanding how it changes is critical for achieving a high RV measurement precision.

These sorts of effects make it incredibly challenging to map our spectra from pixel to wavelength space and calculate precise radial velocity shifts ($\mathrm{RV} = \frac{\Delta\lambda}{\lambda}\, c$, for any given wavelength). Combined with the y position dependence of Schulze (2017) we have been developing a complex wavelength calibration to account for these added variables and test it against known RV standards (Chubak et al. 2012), whose IDs and RVs are listed in Table 3. Before we calculate RVs for the stars in our

sample, the calibration is applied to the RV standards and we calculate their relative RVs, trying to produce the catalog value over the course of one and from night to night. When the measurements accurately reproduce the standards' RVs from night to night, we will apply the calibration to the stars in our sample. Pushing OSMOS to its limits, we hope to ultimately achieve 10-15 km/s precision but currently are at a 20 km/s precision.

For the remainder of summer 2016 I processed and extracted our target and arc spectra and began learning to extract RVs and errors for entire spectra and just portions of it[2]. Once the wavelength calibration improves, I will rerun the spectra through FXCOR to obtain more precise radial velocities.

[2] Iraf.noao.rv.fxcor

3. Analysis

3.1 Spectral Energy Distributions and color based band excesses

We made composite optical-IR SEDs for all 25 of the subgiants in our sample with our own BVRI photometry from MDM, JHK photometry from 2MASS and W1-W4 from WISE. Table 5 lists these bands and their respective wavelengths. None of them showed any W2 or W3 excess, ruling out the presence of a cooler star near the target. Two stars did show excess in W4 (22 μm) but at temperatures that low the excess is likely dust or some sort of systematic error in measuring W4 since these stars do not emit strongly in IR. When compared to the entire 97 subgiant population in the García et al. sample we find a total of four cases with W4 excess, a contamination rate of about 4%. This is consistent with current estimates of excess in solar analogs, twins, and siblings (Da Costa et al. 2017). Figure 7 shows the composite SEDs for the two stars, KIC 08377423 and KIC 09049593, with slight W4 excesses, both normalized to 1 and plotted in units of Jansky (Jy), which is 10^{-26} W m^{-2} Hz^{-1}.

There are eight cases where it looks like there are W4 excesses but the star's emission was so faint in W4 that no magnitude was measured. The values plotted are the upper limits. Figure 8 shows the two cases, KIC 10794845 and KIC 10972252, where we have with no W4 detection. For comparison, figure 9 shows two stars, KIC 03967430 and KIC 09042223, with no excesses detected. Their emission looks approximately like a blackbody. Table 6 lists the W4 classification for each star in our sample: no excess, excess, and no data.

I next searched for W4 excess by plotting our sample on color - color diagrams with the Wu (2013) excess upper limit of K-W4 of 0.21 mag. Figure 10 shows the J-H vs

K-W4 colors of our sample with the Wu (2013) color bound. Eleven stars fell to the right of that line, indicating W4 excess. Two of the 11 stars (black points) actually show excess in their SEDs, seven have no W4 measurement (the magenta points), and the remaining two do not show signs of W4 excess in their SEDs. Objects that emit strongly in W4 are far too cold to be stars, but knowing the W4 excess of our sample is useful for comparisons to the solar neighborhood.

As for our centroid analysis, modeling is still in its initial stages so all we can concretely say is that the RMS shift in position was about 0.07 arcseconds, with the worst nights having shifts about 2 to 3 times as large.

3.2 OSMOS mass sensitivity and RV precision

We achieved precision down to 20 km/s, which we can use to constrain the companion mass. Equation 4 shows the radial RV amplitude of a primary star of mass m_1 as a function of companion mass, m_2, mass ratio, m_1/ m_2, and orbital period P.

$$v_1 \sin i = 70\ kms^{-1} \left(\frac{m_2}{Msun}\right)^{\frac{1}{3}} \left(\frac{1+\frac{m_1}{m_2}}{2}\right)^{-\frac{2}{3}} \left(\frac{P}{7\ days}\right)^{-1/3} \quad (4)$$

Figure 11 shows the detection threshold, m_2 as a function of m_1 and P. The target masses in our sample are about 1.3 – 1.6 solar masses. Each line represents the 20 km/s bound for a given primary mass. With a precision of 20 km/s we can detect companions as small as 0.16 solar masses on orbits near 2 days and 0.27 solar masses on 10 day orbits. Even with less precise radial velocities than hoped for, we can still see most binary systems with only the lowest mass companions being excluded.

Table 6 lists our measured RVs and catalog values for three different RV standards measured over the course of one night. Errors on these measurements are

between 10 and 12 km/s, making it the most accurate data we have. Having that sort of precision would increase our mass sensitivity to 0.07 solar masses at 2 day orbits and 0.11 solar masses at 10 day orbits. For this higher precision, we can see down to approximately the minimum mass required to form a star, making us sensitive to every possible stellar companion.

4. Conclusions

We found no indications of stellar companions in any of the composite SEDs. There were W4 excesses 4% of the time but flux at that wavelength would be from an object, like dust, far too cold to be a star. Since we detected no W2 or W3 excesses it is also possible that there is some sort of systematic error in measuring W4 as many of these stars are faint at 22 μm.

The wavelength calibration for OSMOS has proved to be far more complex than we initially thought, so RV analysis has taken much longer than anticipated. However, we can confidently say that there are no binaries to a precision of 40 km/s. This eliminates most systems, meaning we can proceed with angular momentum transport studies without considering binaries as a major source of contamination. We are also confident that the rapidly rotating population of subgiants in our sample are not in tidally locked binaries. It is possible that higher precision RVs will reveal some low mass binary companions. It is also possible that as we continue with the rest of our photometric analysis we will find some misattributed rotation periods from faint companions. Otherwise, this opens the door to further investigation of rotational spin-down in evolved stars.

5. Future Work

The remaining work consists primarily of going back through the data with higher precision analysis tools and seeing what we find. Once the wavelength calibration is finalized we will recalibrate all the spectra and calculate RV shifts, looking for lower mass companions.

Additionally, we will return to the 35,000 BVRI images, continuing to do photometry on the targets and all the stars within 5" of the target, looking for which star is doing the varying. Since we also have a preliminary understanding of how stars shift in position from exposure to exposure, we are working on automating image stacking from our sets of exposures taken in rapid succession. With these new, higher signal images we will calculate centroid movement from stack to stack.

6. Acknowledgements

I would like to thank Don Terndrup for his continued oversight and guidance for the past two years. Additionally, I owe my thanks to Grace Calhoun, Zach Hartman, and Erika Wagoner who contributed to data collection in 2015 and 2016, and Joe Schulze who contributed to data collection in 2016 and the wavelength calibration.

7. References

Atkinson, D., Baranec, C., Ziegler, C. 2017, AJ, 153, 25

Barnes, S. A. 2003 ApJ, 586, 464–479

Barnes, S. A., Weingrill, J., Fritzewski, D. 2016, ApJ, 823, 16

Chubak, C., Marcy, G.; Fischer, D. A., et al. 2012, arXiv:1207.6212

Da Costa, A. D., Canto Martins, B. L., Leão, I. C., et al., 2017, ApJ, 837, 15

Dalba, P. A, Muirhead, P. S., Croll, B., Kempton, E. M. R. 2017, AJ, 153, 59

Epstein, C. R., Pinsonneault, M. H. 2014, ApJ, 780, 159

García, R. A., Ceillier, T., Salabert, D., et al. 2014, A&A, 572, A34

Landolt, A. U. 2007, ASPC, 364, 27

Matt, S. P., MacGregor, K. B., Pinsonneault, M. H., & Greene, T. P. 2012, ApJL, 754, L26

Schulze, J. 2017, Senior Thesis, The Ohio State University

Skumanich, A. 1972, ApJ, 171, 565

van Saders, J. L., Pinsonneault, M. H. 2013, ApJ, 776, 67

van Saders, J. L., Pinsonneault, M. H., García, R. A., Ceillier, T. 2015, EPJWC , 101, 05006

Table 1 – A list of the stars used in this study with the type data we have for each

SED	Spectrum	KIC ID	RA (J200)	DEC (J200)	Prot	err
x	x	1435467	19 28 19.85	+37 03 35.32	6.68	0.89
x	x	3223000	19 11 51.050	+38 23 43.87	4.85	0.39
x	x	3424541	19 00 42.98	+38 34 24.85	3.46	0.33
x	x	3761840	19 40 41.99	+38 48 08.24	3.92	0.29
x	x	3967430	19 39 26.83	+39 00 42.70	2.25	0.17
x	x	4638884	19 05 37.88	+39 43 09.88	6.46	0.85
x	x	4756112	19 37 30.55	+39 51 20.41	5.43	0.46
x	x	5371516	19 37 27.69	+40 35 19.86	5.23	0.48
x	x	5689219	19 03 46.96	+40 55 14.30	0.98	0.07
x	x	5773155	19 01 23.58	+41 01 11.89	7.51	0.9
x	x	6232600	19 55 29.19	+41 34 59.81	6.52	0.87
x	x	6448798	19 34 55.039	+41 53 56.76	6.44	0.56
x		6853020	19 14 41.61	+42 20 33.61	4.82	0.42
x	x	8289241	19 10 30.56	+44 16 51.02	7.96	0.71
x	x	8377423	19 43 42.28	+44 18 41.04	11.39	0.98
x	x	8579578	19 52 41.60	+44 36 16.85	3.81	0.65
x	x	9049593	19 59 09.92	+45 23 29.69	12.36	2.55
x	x	9226926	19 40 27.17	+45 41 45.96	2.17	0.15
x	x	9402223	19 24 21.95	+45 58 18.16	4.87	0.89
x	x	9414417	19 43 12.64	+45 59 17.09	10.68	0.66
x		9579208	19 10 33.021	+46 12 15.88	5.39	0.59
x	x	9715099	19 35 23.73	+46 26 01.10	4.81	0.46
x		10016239	19 35 05.16	+46 58 29.42	4.91	0.39
x		10794845	19 23 29.60	+48 06 52.92	1.4	0.08
x	x	10972252	19 20 14.28	+48 25 46.38	12.63	0.97

Table 2 – A list of Landolt equatorial standards used for photometric calibration. Here T denotes the primary star.

Star	RA	DEC	V	B-V	V-R	V-I
PG1323A	13 25 49	-08 50 24	13.59	0.393	0.252	0.506
PG1323B	13 25 50	-08 51 55	13.41	0.761	0.426	0.833
PG1323C	13 25 50	-08 48 39	14.00	0.707	0.395	0.759
PG1323T	13 25 39	-08 49 18	13.48	-0.140	-0.048	-0.127
PG1633A	16 35 26	+09 47 48	15.26	0.873	0.505	1.015
PG1633B	16 35 34	+09 46 17	12.97	1.081	0.590	1.090
PG1633C	16 35 38	+09 46 11	13.23	1.134	0.618	1.138
PG1633D	16 35 40	+09 46 38	13.69	0.535	0.324	0.650
PG1633T	16 35 24	+09 47 45	14.40	-0.192	-0.093	-0.212
PG1657A	16 59 33	+07 42 19	14.03	1.069	0.573	1.113
PG1657B	16 59 32	+07 42 05	14.72	0.708	0.417	0.838
PG1657C	16 59 35	+07 42 20	15.23	0.840	0.521	0.967
PG1657T	16 59 32	+07 43 25	15.02	-0.149	-0.063	-0.100

Table 3 – Catalog and measured colors for Landolt equatorial standards

Name	V	B-V	V-R	V-I	v	b-v	v-r	v-i
PG1323A	13.590	0.393	0.252	0.506	13.516	0.423	0.234	0.498
PG1323C	14.000	0.707	0.395	0.759	13.990	0.712	0.388	0.750
PG1323T	13.480	0.140	0.048	0.127	13.501	0.131	0.056	0.135
PG1633B	12.970	1.081	0.590	1.090	12.944	1.107	0.593	1.098
PG1633C	13.230	1.134	0.618	1.138	13.202	1.140	0.617	1.141
PG1633D	13.690	0.535	0.324	0.650	13.680	0.572	0.327	0.675
PG1633T	14.400	0.192	0.093	0.212	14.415	0.224	0.095	0.183
PG1633A	15.260	0.873	0.505	1.015	15.264	0.892	0.489	1.001
PG1633T	14.400	0.192	0.093	0.212	14.407	0.198	0.087	0.184
PG1633A	15.260	0.873	0.505	1.015	15.293	0.886	0.496	1.014
PG1633B	12.970	1.081	0.590	1.090	12.974	1.081	0.601	1.094
PG1633C	13.230	1.134	0.618	1.138	13.261	1.127	0.607	1.129
PG1633D	13.690	0.535	0.324	0.650	13.695	0.531	0.323	0.671
PG1657T	15.020	0.149	0.063	0.100	15.000	0.161	0.071	0.121
PG1657A	14.030	1.069	0.573	1.113	14.035		0.569	1.119
PG1657B	14.720	0.708	0.417	0.838	14.714	0.699	0.426	0.847
PG1657C	15.230	0.840	0.521	0.967	15.206	0.852	0.477	0.959
PG1657T	15.020	0.149	0.063	0.100	15.002	0.163	0.057	0.130
PG1657A	14.030	1.069	0.573	1.113	14.010		0.587	1.090
PG1657B	14.720	0.708	0.417	0.838	14.730	0.699	0.435	0.853
PG1657C	15.230	0.840	0.521	0.967	15.222	0.839	0.497	0.963
PG1633B	12.970	1.081	0.590	1.090	12.959	1.079	0.604	1.082
PG1633C	13.230	1.134	0.618	1.138	13.249	1.123	0.611	1.125
PG1633D	13.690	0.535	0.324	0.650	13.701	0.535	0.355	0.679
PG1657T	15.020	0.149	0.063	0.100	15.012	0.173	0.070	0.122
PG1657A	14.030	1.069	0.573	1.113	14.051		0.579	1.119
PG1657B	14.720	0.708	0.417	0.838	14.729	0.689	0.418	0.839
PG1657C	15.230	0.840	0.521	0.967	15.223	0.840	0.482	0.961

Table 4 – A list of the RV standards used for our wavelength calibration

Star	RA	DEC	RV (km/s)	err
HD 088230	10 11 22.14	+49 27 15.26	-25.73	0.1
HD 132142	14 55 11.043	+53 40 49.26	-14.69	0.04
HD 157214	17 20 39.56	+32 28 03.68	-78.53	0.08
HD 182572	19 24 58.20	+11 56 39.89	-100.25	0.09
HD 187923	19 52 03.44	+11 37 41.98	-20.56	0.09
HD 188512	19 55 18.79	+06 24 24.34	-40.07	0.09

Table 5 – Wavelengths of the Optical-IR bands

Band	λ (μm)
B	0.44
V	0.55
R	0.64
I	0.79
J	1.24
H	1.66
K	2.16
W1	3.35
W2	4.60
W3	11.56
W4	22.09

Table 6 – A list of the type of W4 detection for each star

KIC ID	No W4 excess	W4 excess	No data
1435467	x		
3223000	x		
3424541	x		
3761840			x
3967430	x		
4638884	x		
4756112			x
5371516	x		
5689219	x		
5773155			x
6232600	x		
6448798			x
6853020			x
8289241	x		
8377423		x	
8579578	x		
9049593		x	
9226926	x		
9402223	x		
9414417	x		
9579208			x
9715099	x		
10016239	x		
10794845			x
10972252			x

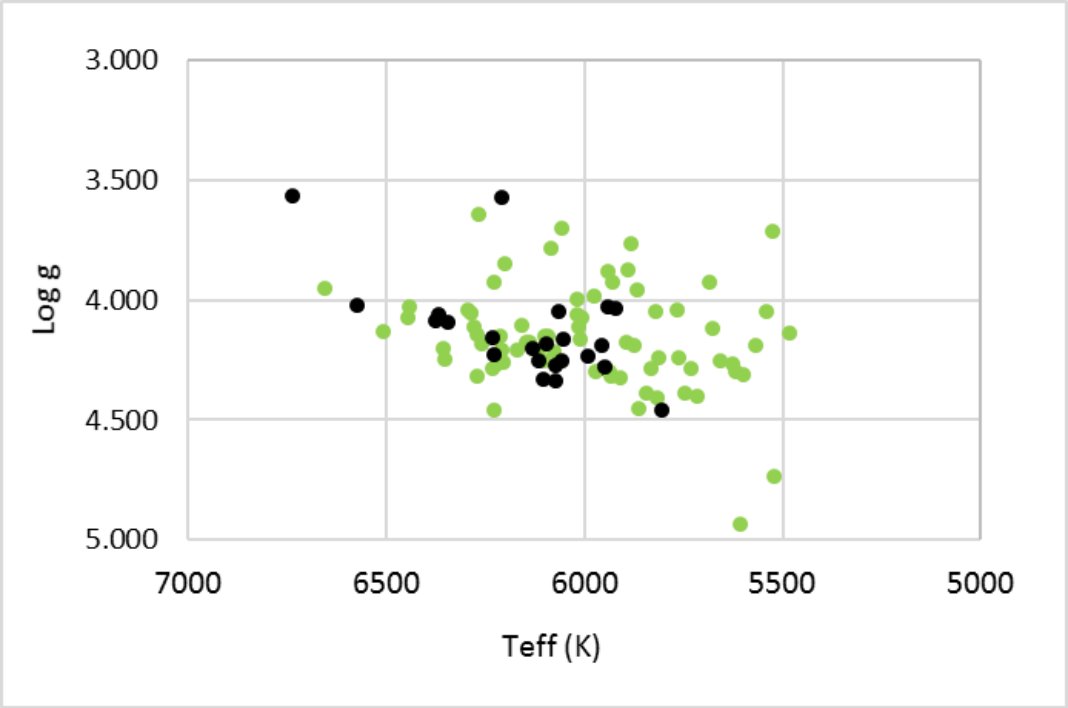

Figure 1 – A plot of log g vs T_{eff} of all of the subgiants in the García et al sample (green points). Black points represent the 25 stars in our sample.

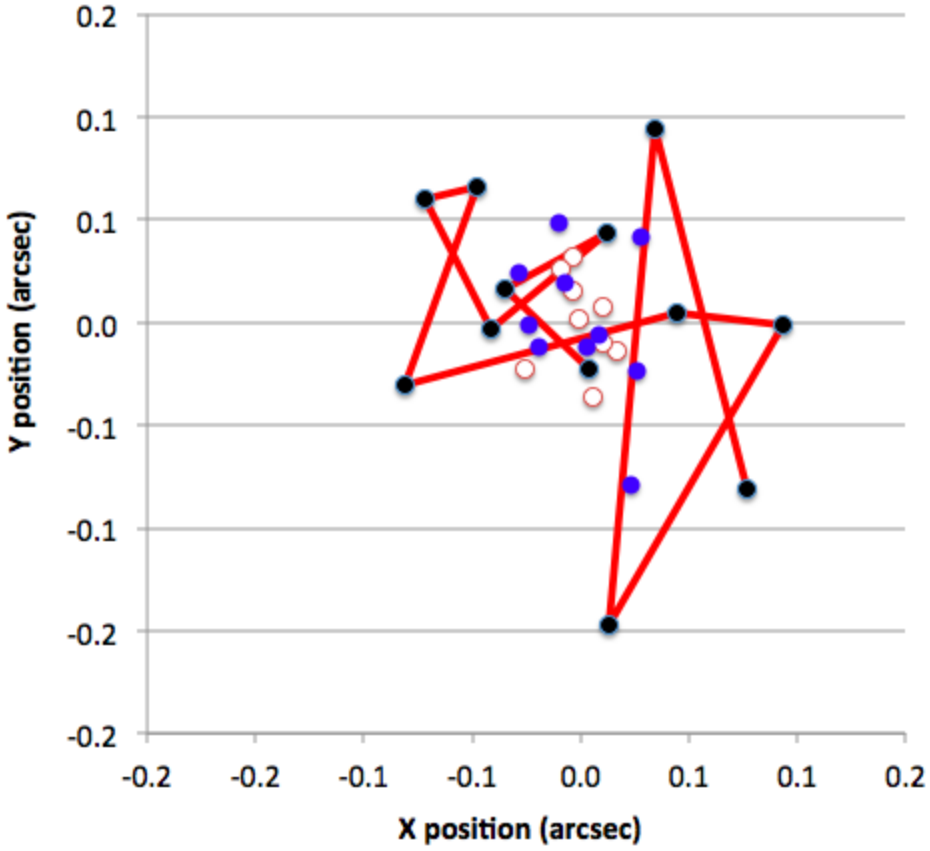

Figure 2 – X versus Y shifts in position from UT 06 13 2015 and UT 06 14 2015. The connected black points represent the worst position shifts we see. They are from KIC 057331516 and imaged with a seeing of 2.21 arcseconds. The blue and white points represent the RMS position shifts (0.07 arcseconds) we see, here in KIC 06853020 and KIC 10016239. Seeing was 2.1 arcseconds. All images were taken in the V filter.

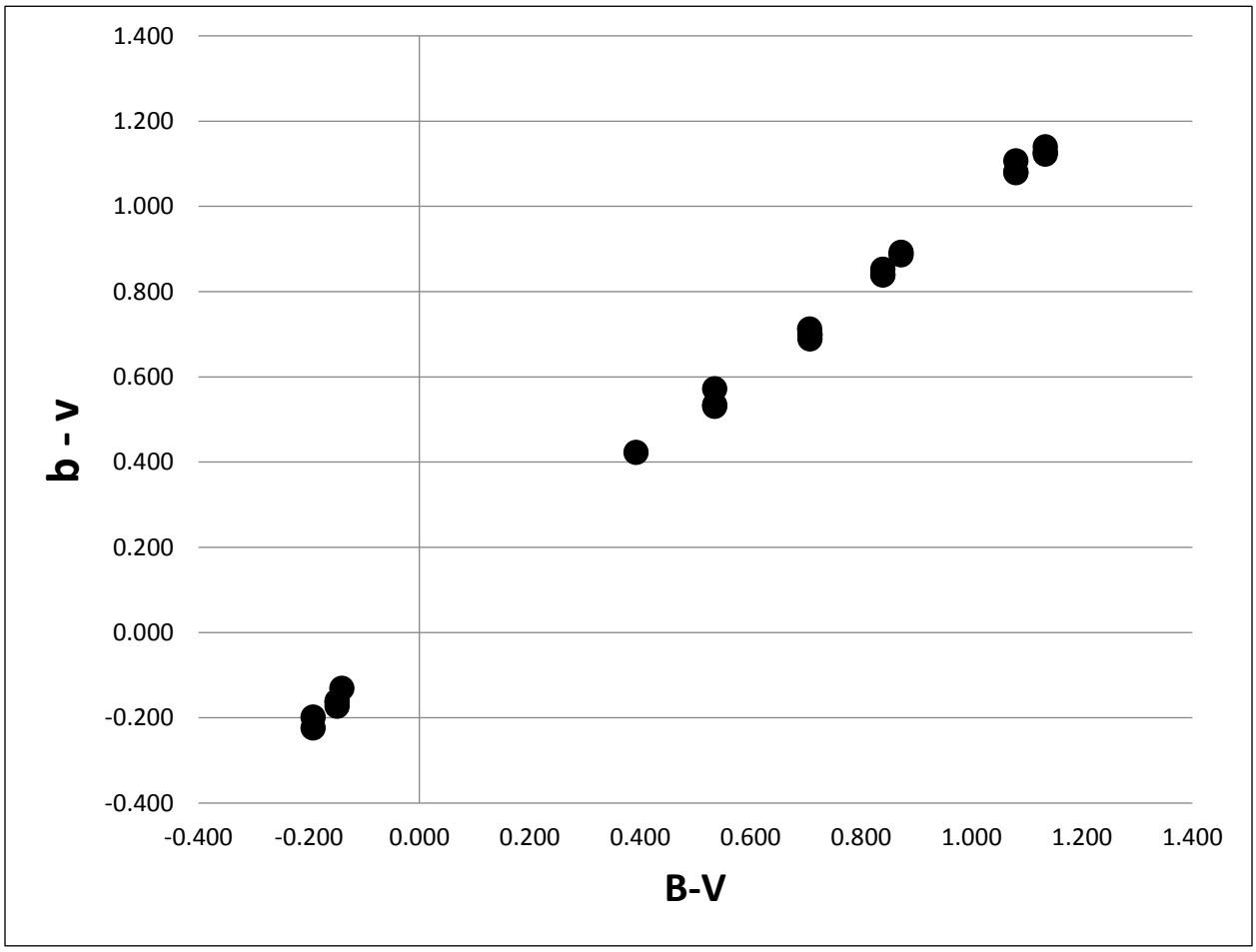

Figure 3 – A plot of measured b-v versus B-V cataloged color

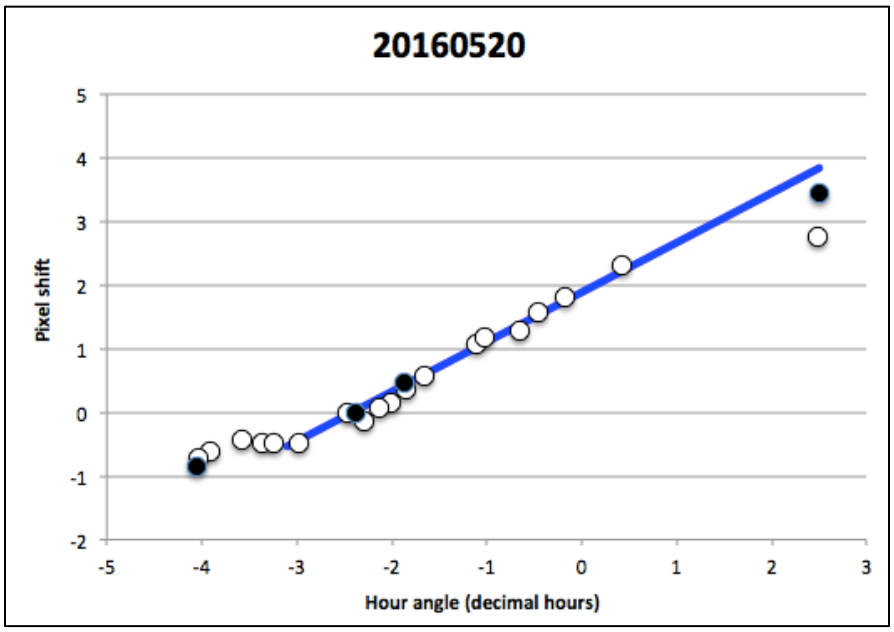

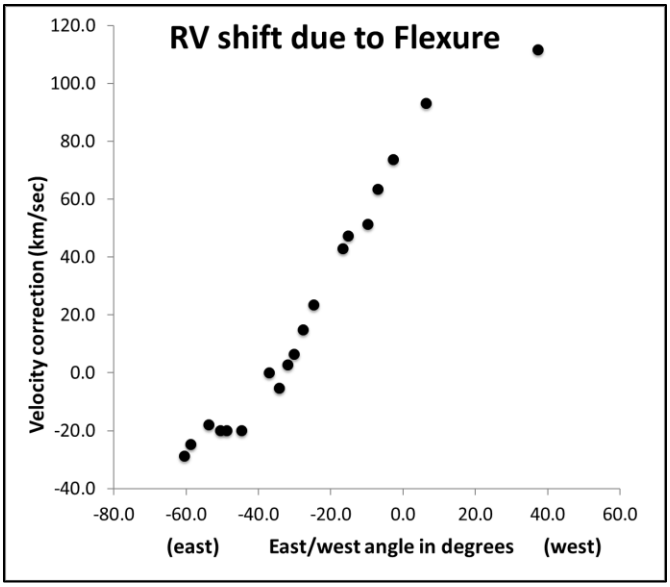

Figure 4 – The top panel shows the pixel shift as the spectrograph changed position, measured by Hour Angle. The date at the top is the date from which the data come. Filled points represent Hg-Ne lines and open points represent the Telluric line. The bottom panel shows the corresponding RV corrections to pixel shifts now plotted over degrees.

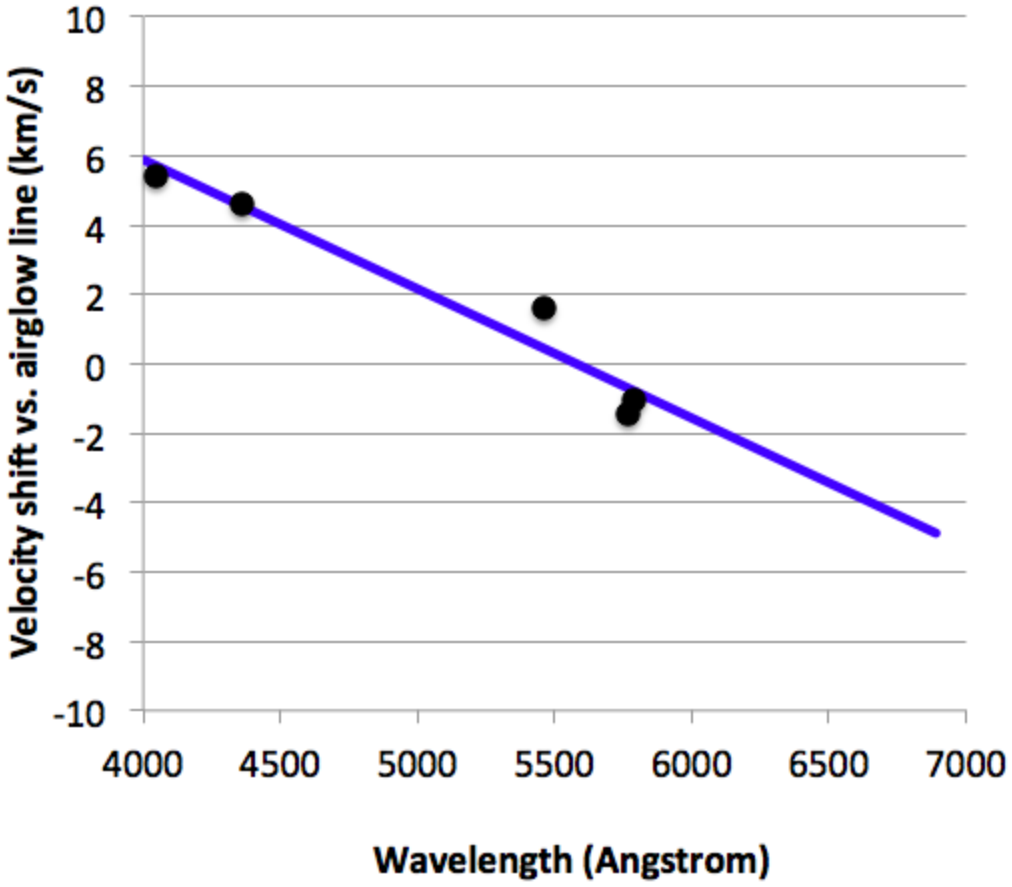

Figure 5 – A plot of the five main emission features of an Hg-Ne arc lamp and their residual radial velocities after flexure corrections were made. The effects are clearly wavelength-dependent.

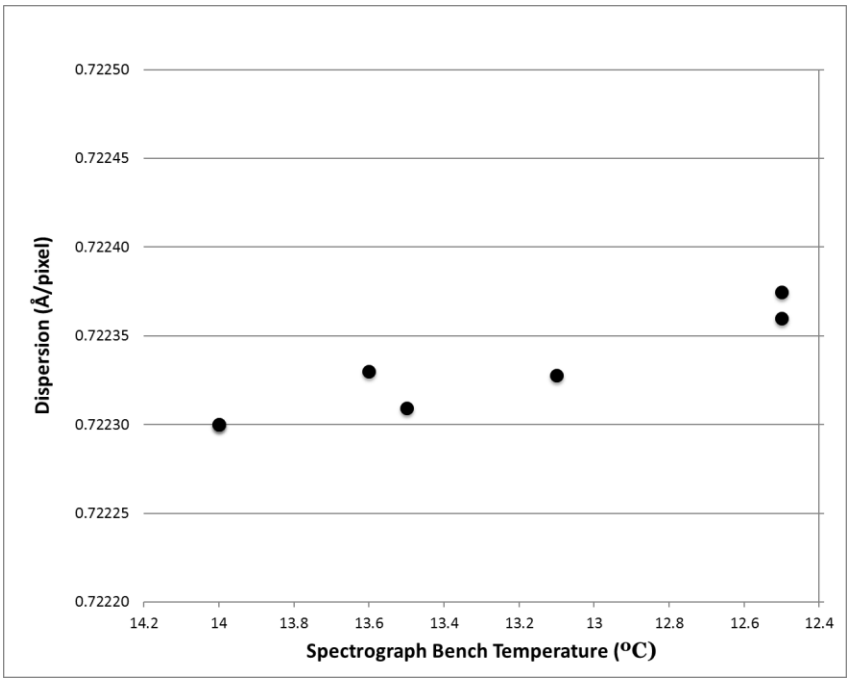

Figure 6 – The top panel shows how dispersion changes with spectrograph temperature. The bottom panel shows dispersion as a function of camera focus. Both have linear relationships.

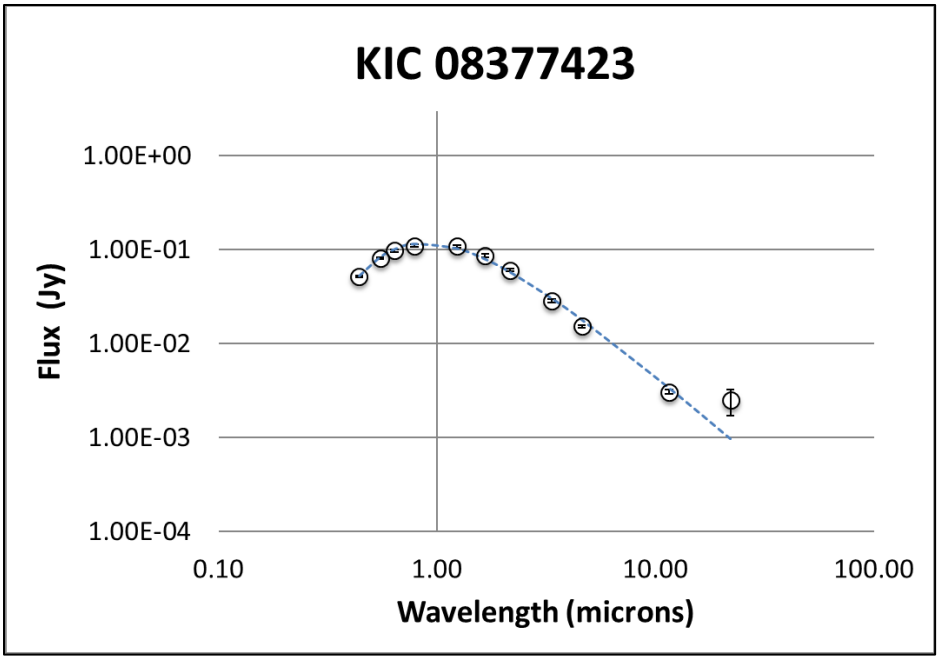

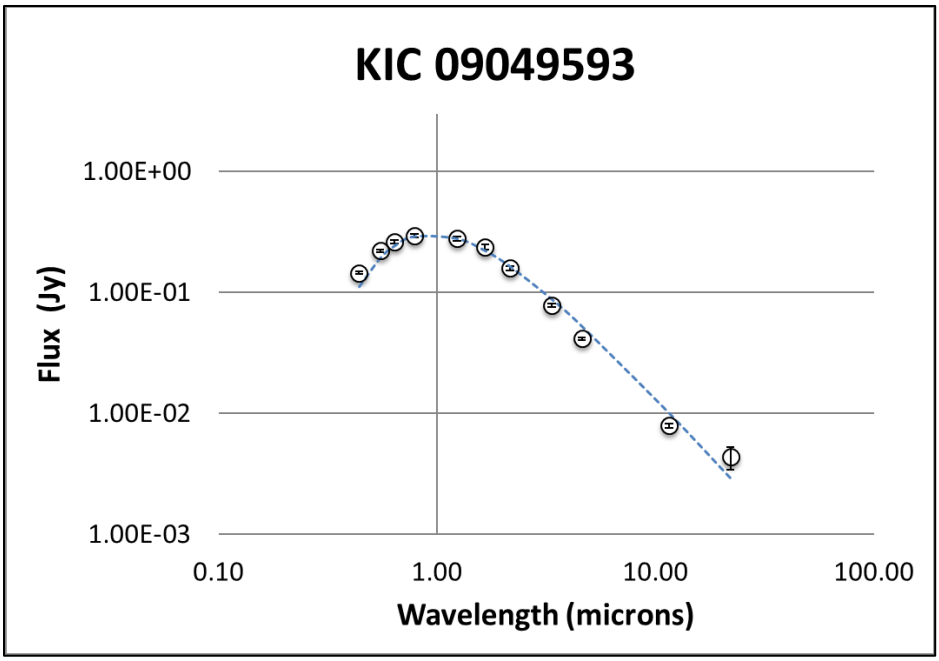

Figure 7 – Composite SEDs (BVRI on the right) for two stars where W4 excess is present. The blue dashed line represents the simulated blackbody curve for a star of the same T_{eff}.

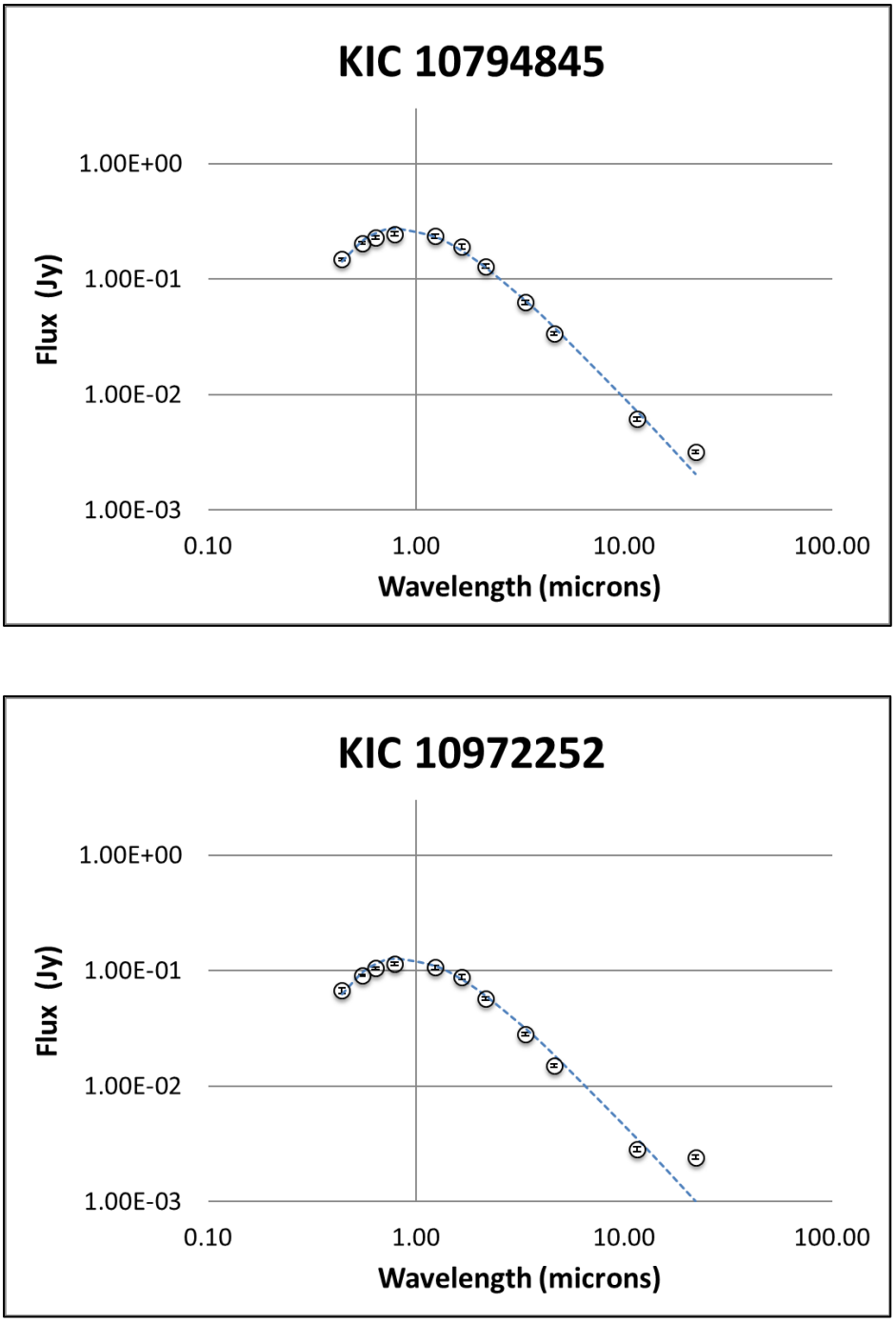

Figure 8 – Composite SEDs (BVRI on the right) for two stars where there is no W4 magnitude. The blue dashed line represents the simulated blackbody curve for a star of the same T_{eff}.

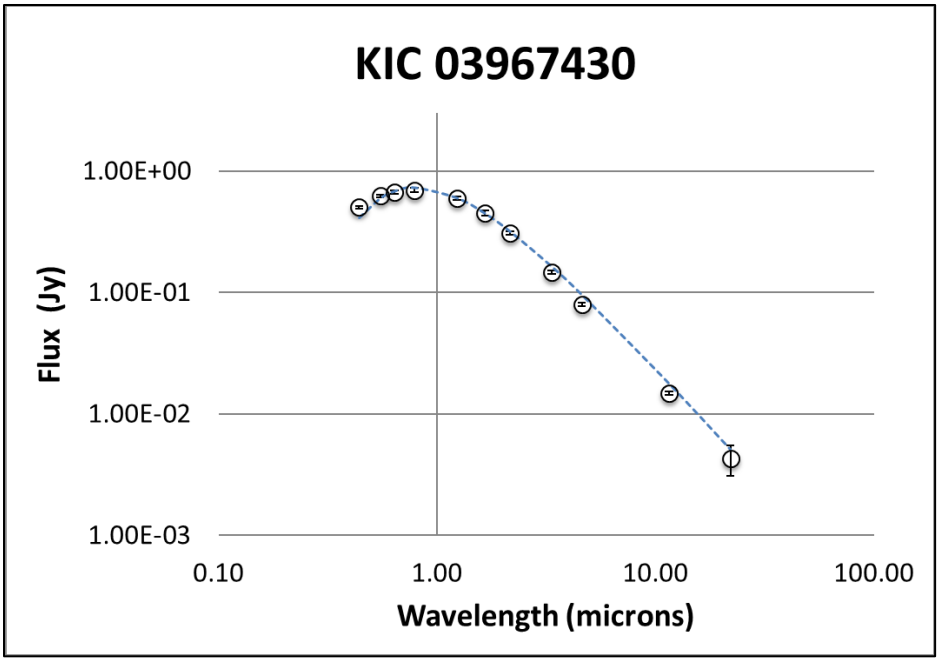

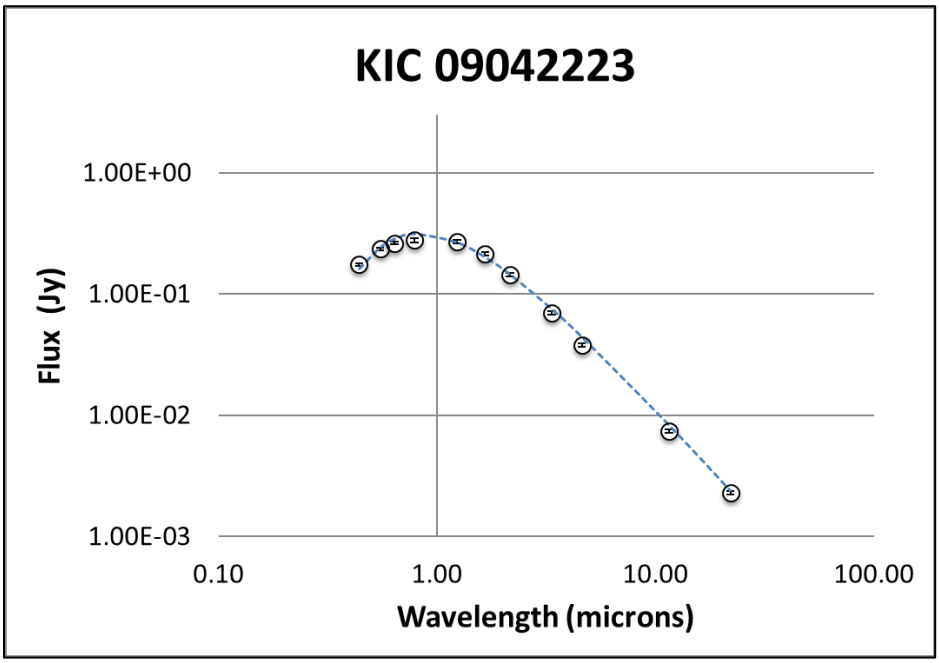

Figure 9 – Composite SEDs (BVRI on the right) for two stars where no excess is present in any band. The blue dashed line represents the simulated blackbody curve for a star of the same T_{eff}.

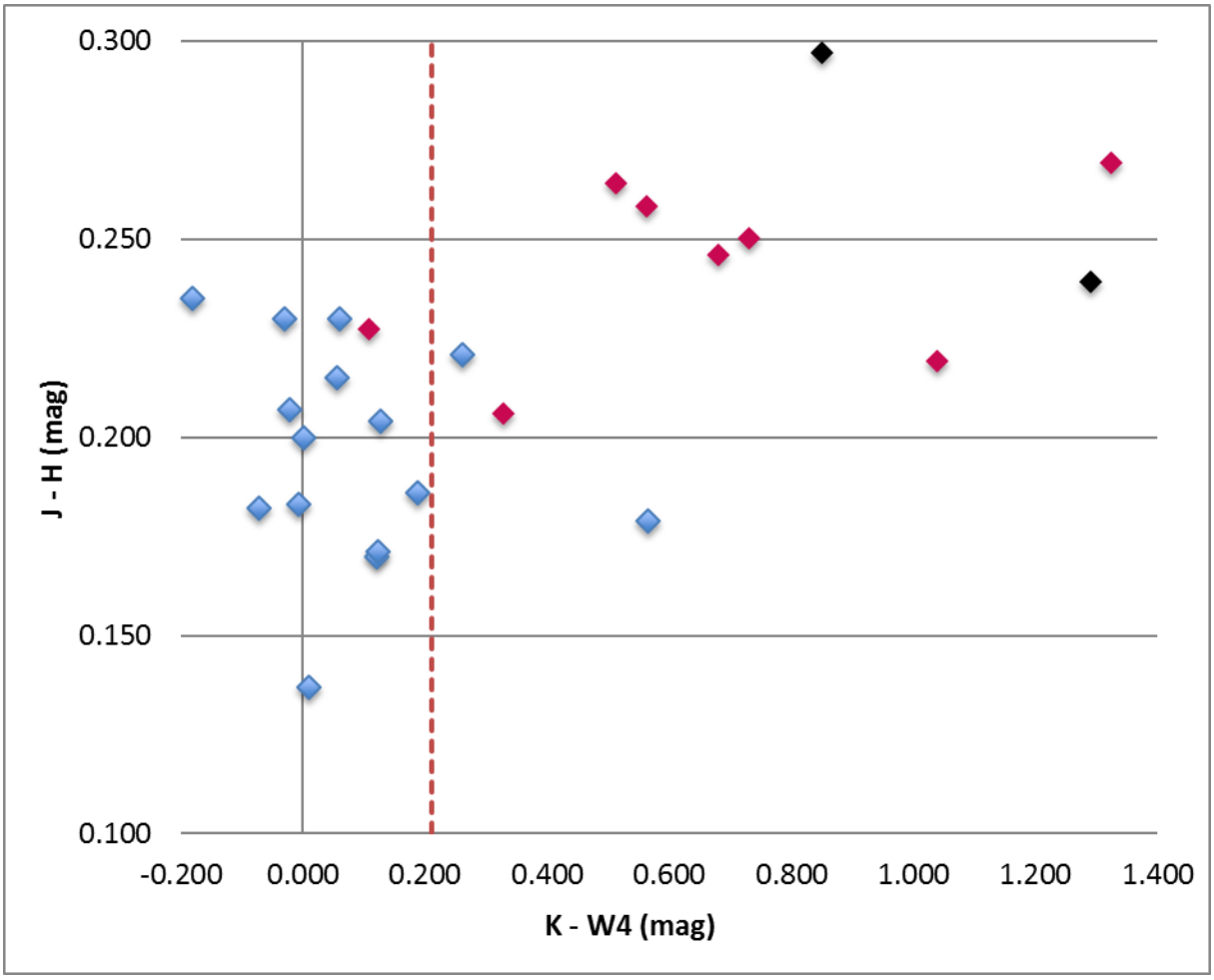

Figure 10 – A color-color plot of J-H vs K-W4 for all of our stars. Blue points are stars with W4 measurements, black points represent the two stars with W4 excess in their SEDs and magenta points are stars with no W4 measurement. The red dashed line represents the Wu (2013) upper color limit. Anything to the right of that line indicates W4 excess.

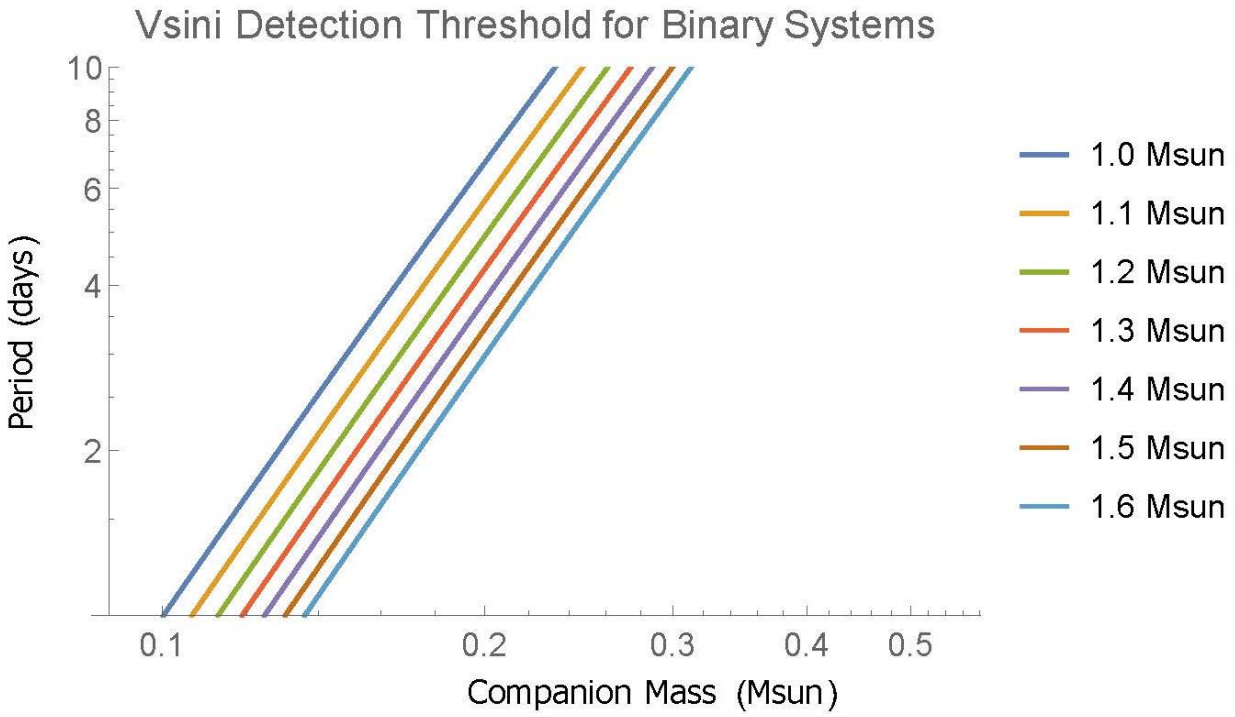

Figure 11 - A plot of period, at fixed primary mass, as a function of companion mass and mass ratio. Each line represents the 20 km/s bound for the respective primary mass. Every system with a companion mass to the right of the line is detectable by our spectrograph.